nature materials

Article

https://doi.org/10.1038/s41563-024-01998-7

Origins of enhanced oxygen reduction activity of transition metal nitrides

Received: 27 March 2023

Accepted: 8 August 2024

Published online: 03 September 2024

Check for updates

Rui Zeng[1,7], Huiqi Li[1,7], Zixiao Shi[1,7], Lang Xu[2,7], Jinhui Meng[3], Weixuan Xu[1], Hongsen Wang[1], Qihao Li[1], Christopher J. Pollock[4], Tianquan Lian[3] ✉, Manos Mavrikakis[2] ✉, David A. Muller[5,6] ✉ & Héctor D. Abruña[1] ✉

Transition metal nitride (TMN-) based materials have recently emerged as promising non-precious-metal-containing electrocatalysts for the oxygen reduction reaction (ORR) in alkaline media. However, the lack of fundamental understanding of the oxide surface has limited insights into structure–(re)activity relationships and rational catalyst design. Here we demonstrate how a well-defined TMN can dictate/control the as-formed oxide surface and the resulting ORR electrocatalytic activity. Structural characterization of MnN nanocuboids revealed that an electrocatalytically active Mn_3O_4 shell grew epitaxially on the MnN core, with an expansive strain along the [010] direction to the surface Mn_3O_4. The strained Mn_3O_4 shell on the MnN core exhibited an intrinsic activity that was over 300% higher than that of pure Mn_3O_4. A combined electrochemical and computational investigation indicated/suggested that the enhancement probably originates from a more hydroxylated oxide surface resulting from the expansive strain. This work establishes a clear and definitive atomistic picture of the nitride/oxide interface and provides a comprehensive mechanistic understanding of the structure–reactivity relationship in TMNs, critical for other catalytic interfaces for different electrochemical processes.

The design and synthesis of electrocatalysts for the sluggish oxygen reduction reaction (ORR) is critical to advancing hydrogen fuel cells for transportation electrification[1]. However, most ORR electrocatalysts developed for proton exchange membrane fuel cells require platinum and/or other precious metals[2]. The expansion of current fuel-cell electric vehicles (~30 g_{Pt} per vehicle)[3] with an annual production level of 80 million units is projected to consume over 2,400 tons of Pt yearly, over ten times more than current Pt production capacity[4]. In contrast to proton exchange membrane fuel cells, anion exchange membrane fuel cells (AEMFCs) enable the use of precious-metal-free catalysts, since operating at high pH markedly mitigates electrocatalyst corrosion[5]. Thus, the ability to incorporate non-precious-metal catalysts will enable AEMFCs to markedly reduce overall costs, offering a promising solution for next-generation fuel-cell-powered vehicles[6,7].

A broad range of transition metal oxides have been investigated as ORR catalysts in alkaline media[8–17]. However, the intrinsic semiconductive nature of most metal oxide materials has limited charge transfer kinetics and further activity enhancements[10,18,19]. Transition metal nitrides (TMNs) have received increasing attention due to their high electronic conductivity, especially when compared with their

[1]Department of Chemistry and Chemical Biology, Cornell University, Ithaca, NY, USA. [2]Department of Chemical & Biological Engineering, University of Wisconsin–Madison, Madison, WI, USA. [3]Department of Chemistry, Emory University, Atlanta, GA, USA. [4]Cornell High Energy Synchrotron Source, Wilson Laboratory, Cornell University, Ithaca, NY, USA. [5]School of Applied and Engineering Physics, Cornell University, Ithaca, NY, USA. [6]Kavli Institute at Cornell for Nanoscale Science, Cornell University, Ithaca, NY, USA. [7]These authors contributed equally: Rui Zeng, Huiqi Li, Zixiao Shi, Lang Xu.
✉e-mail: tlian@emory.edu; emavrikakis@wisc.edu; david.a.muller@cornell.edu; hda1@cornell.edu

https://doi.org/10.1038/s41563-024-01998-7

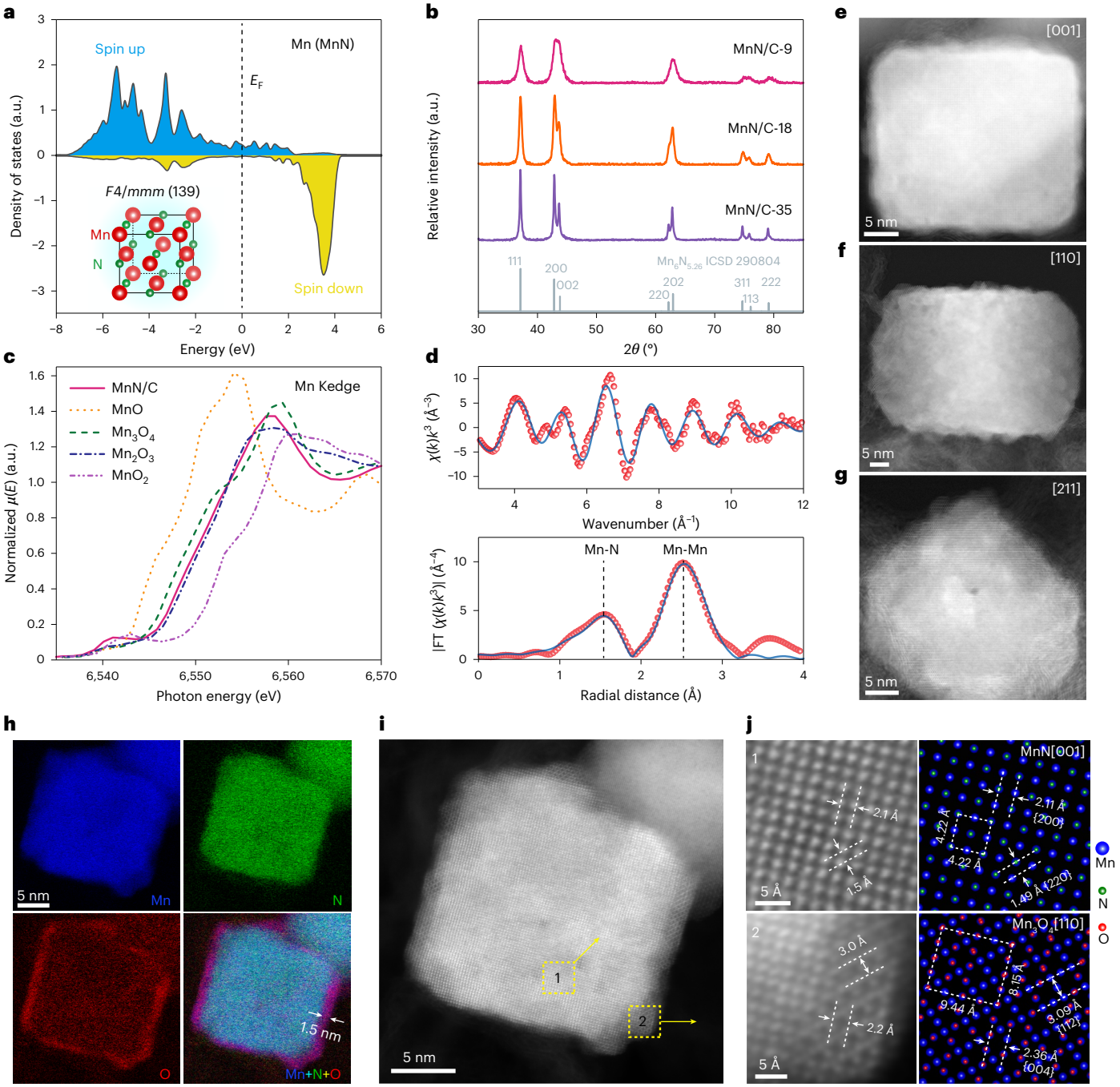

Fig. 1 | Physicochemical characterization of as-synthesized MnN/C catalysts. **a**, Calculated density of states of Mn for MnN. MnN is metallic with electronic bands crossing the Fermi level (E_F, denoted by the dashed line). Inset: atomic arrangement model of MnN with an fcc configuration. **b**, XRD patterns of as-synthesized carbon-supported MnN NPs compared with reference patterns from the Inorganic Crystal Structure Database (ICSD). MnN/C-9, MnN/C-18 and MnN/C-35 represent MnN/C samples with grain sizes of 9, 18 and 35 nm, respectively. **c**, Mn K-edge XANES spectra of MnN/C, compared with those of Mn oxide references. The edge shape of MnN/C is consistent with that of Mn(III). **d**, k^3-weighted EXAFS spectra (upper panel) and corresponding FTs (lower panel) of EXAFS (points) and fit (line) for MnN/C, shown in k space and R space (FT magnitude) without phase correction. The dashed lines correspond to the first two coordination shells, Mn–N and Mn–Mn, respectively. **e**–**g**, STEM images of cuboidal MnN NPs viewed with different projections. **h**, EELS elemental mapping of Mn, N, O and their composite, displaying typical core/shell structure with the nitride core covered by a ~1.5-nm-thick oxide shell. **i**,**j**, Atomic-scale STEM images of a MnN NP with core (1) and shell (2) regions corresponding to MnN and Mn_3O_4, as confirmed by corresponding d spacings and symmetry consistent with crystal models projected from MnN [001] and Mn_3O_4 [110]. The dashed rectangles in the atomic models denote the smallest repeating units of the crystal structures. a.u., arbitrary units.

oxide counterparts[20,21]. The tendency of TMNs to undergo surface oxidation, forming a nitride-core/oxide-shell structure, has been recognized as a viable approach to circumvent the conductivity challenges and enhance oxygen electrocatalysis[22–24]. While considerable efforts have been dedicated to advancing TMNs as efficient ORR electrocatalysts[25–30], it remains unclear how the nitride core interacts with the surface oxide to impact its ORR activity. This is primarily because previous studies generally refer to the surface oxide simply as MO_x without a clear understanding as to whether the oxide layer is crystalline or amorphous, to which phase it belongs, how it grows on top of

the original nitride or what kind of influence the nitride core probably exerts on it. This knowledge gap has impeded our efforts to advance a complete understanding of the structure–(re)activity relationships of TMNs and gain additional insights into rational catalyst design.

Here, we resolve the atomic structure of the nitride-core/oxide-shell interface and unveil the underlying mechanism(s) for controlling the ORR performance, based on well-defined manganese nitride nanoparticles (NPs) as a model catalyst. Extensive physicochemical characterization suggested that the as-prepared cuboidal MnN NPs consist of a natively formed ~1.5-nm-thick Mn_3O_4 shell around the nitride core. Furthermore, rigorous electrochemical investigations indicated that the metal nitride core played a key role in outperforming the spinel oxide counterparts. Operando studies showed that the surface spinel oxide contributed to, and is probably responsible for, the observed ORR activity, and that the nitride structure could be maintained above a threshold potential. Strain analysis, based on advanced electron microscopy, suggested that the MnN core exerted an expansive strain along [010] on the epitaxially grown Mn_3O_4 surface. Density functional theory (DFT) calculations revealed that such an expansively strained Mn_3O_4 surface could strengthen the OH binding and result in a more hydroxylated surface, which in turn probably enhanced the ORR kinetics. This work clarifies the nature of the oxide surface in TMNs and identifies underlying factors governing the ORR performance of TMNs based on a well-defined model catalyst. Our work thus emphasizes the need for atomistic insights into other similar core/shell-structured catalysts for other energy technologies/applications.

Physicochemical characterization

Among the four stable Mn–N phases[31], MnN with an ideal Mn:N composition ratio of 1:1 was chosen as it represents the most thermodynamically favourable phase[32]. DFT calculations suggest that MnN is metallic (Fig. 1a), thus providing a great advantage over its semi/non-conductive oxide counterpart (band gap of ~0.9 eV; Supplementary Fig. 1) for electrochemical applications. The X-ray diffraction (XRD) patterns in Fig. 1b and Supplementary Fig. 2 indicate that the as-synthesized MnN adopted a distorted NaCl-type face-centred cubic structure (Fig. 1a inset, space group $F4/mmm$, $a = b = 4.219$ Å, $c = 4.129$ Å)[33]. The domain size can be tuned from 35 nm to 18 nm and further down to 9 nm (denoted as MnN/C-35, MnN/C-18 and MnN/C-9; Supplementary Table 1). The Mn K-edge X-ray absorption near-edge structure (XANES) spectra of MnN/C presented a distinct pre-edge feature at ~6,541 eV (Fig. 1c), corresponding to a transition from the core level 1*s* to the vacant 3*d* orbitals, rendered by the Jahn–Teller distortion of the octahedral structural units[34,35]. The Fourier transforms (FTs) of the extended X-ray absorption fine-structure (EXAFS) spectra displayed Mn–N and Mn–Mn coordination shells (Fig. 1d) at interatomic distances of 2.03 Å and 2.97 Å and with coordination numbers of 4.9 and 9.3 (Supplementary Fig. 3, Supplementary Table 2), consistent with the crystal arrangement in MnN.

The morphology and microstructure of the as-synthesized MnN/C catalysts were examined with scanning transmission electron microscopy (STEM). As indicated in Fig. 1e–g, atomically resolved STEM images of a MnN NP along [001], [110] and [211] zone axes revealed its cuboidal shape. The average particle sizes of MnN NPs were estimated to be 9, 18 and 34 nm for MnN/C-9, MnN/C-18 and MnN/C-35, respectively (Supplementary Figs. 4–6), consistent with the XRD domain analysis (Supplementary Table 1). The chemical distribution of MnN NPs was revealed by elemental mapping derived from electron energy loss spectroscopy (EELS) spectra (Fig. 1h and Supplementary Fig. 7). As presented in Fig. 1h, Mn and N are uniformly distributed in the particle, while oxygen is enriched near the particle surface with a thickness of ~1.5 nm. This feature was validated by more detailed elemental analyses (Supplementary Figs. 8 and 9). The atomic-scale structures of MnN NPs were examined by aberration-corrected, high-angle annular dark-field STEM (Fig. 1i,j). The ordered arrays of distinct bright atoms inside the particle displayed four-fold symmetry and *d*-spacing values of 2.1 Å and 1.5 Å, matching well with the atomic configurations along the [001] zone axis in a MnN crystal model. However, the surface region showed an atomic arrangement characteristic of Mn_3O_4, with *d* spacings of the Mn_3O_4{112} (3.0 Å) and Mn_3O_4{004} planes (2.2 Å), consistent with a projection viewed from the [110] zone axis in a Mn_3O_4 crystal model. These observations unambiguously established that the particle consists of a thin Mn_3O_4 shell and a bulk MnN core.

Electrocatalytic evaluation

The electrochemical performance of MnN/C (20 wt%) was evaluated via rotating disc electrode (RDE) measurements in 1.0 M KOH solution. The voltammetric profiles of MnN/C catalysts exhibited pronounced Mn(II)/(III) redox features at around 0.90 V versus a reversible hydrogen electrode (RHE) (Fig. 2a), more negative than that of Mn_3O_4/C (Supplementary Figs. 10 and 11). The peak current density scaled linearly with scan rate (Supplementary Figs. 12–14), indicating a surface redox process. From the integrated current, that is, the coulometric charge (Fig. 2b and Supplementary Fig. 11), we were able to calculate the electrochemical surface area[36]. When evaluated in an O_2-saturated electrolyte, MnN/C catalysts displayed a well-defined diffusion-limited current density (j_{lim}) converging to 3.75 mA cm^{-2} at 1,600 r.p.m., suggesting a dominant four-electron reduction process (Fig. 2c)[37–39]. When compared with Mn_3O_4/C, MnN/C catalysts exhibited improved ORR activity, with MnN/C-9 displaying the highest mass activity (MA) at ~266 A g^{-1} and a half-wave potential ($E_{1/2}$) of 0.870 V versus RHE (Fig. 2d and Supplementary Table 3). We note that MnN is among the most active Mn-based oxide catalysts for alkaline ORR reported so far (Supplementary Fig. 15). We also observe that the surface redox charge normalized ORR activities (intrinsic activities) were over 300% higher than that of Mn_3O_4/C but virtually the same for the three MnN/C catalysts despite their different particle sizes (Fig. 2d), suggesting that the surface oxide of the MnN NPs is largely responsible for the observed ORR performance. Moreover, MnN/C catalysts showed a much higher redox charge density when compared with Mn_3O_4/C (Supplementary Fig. 16 and Supplementary Table 3), indicating that the conductive MnN core enables access to a larger fraction of active sites. While Mn_3O_4/C displayed substantial H_2O_2 yield (~9%), MnN/C-18 maintained exceptionally high four-electron selectivity, with H_2O_2 yields of less than 4% (Fig. 2e), approaching the value of Pt/C (3–4%; Supplementary Fig. 17). MnN/C catalysts also displayed impressive ORR stability under accelerated durability testing with an $E_{1/2}$ decay of 8 mV after 10,000 potential cycles (Supplementary Figs. 18–20).

To validate the effectiveness of MnN/C in H_2–O_2 fuel cells, 60 wt% MnN/C (Supplementary Fig. 21) was employed as the cathode catalyst in a membrane electrode assembly[40] and compared with 60 wt% Mn_3O_4/C. As shown in Fig. 2f, the MnN/C cathode displayed an open-circuit voltage of ~0.90 V, higher than that of Mn_3O_4/C (0.85 V). Moreover, MnN/C outperformed Mn_3O_4/C with a peak power density of 884 mW cm^{-2} at 1.5 A cm^{-2}. We expect that further optimization of the particle size and weight percentage of MnN/C could maximize active sites, facilitate mass transport and thus improve overall fuel cell performance[41].

Operando/in situ spectroscopic study

Operando synchrotron-based X-ray absorption spectroscopy (XAS) was employed to investigate the activity and structural stability of MnN/C catalysts under electrochemical conditions (Fig. 3a–d and Supplementary Fig. 22). As shown in Fig. 3a, the Mn K edge shifted negatively by ~1 eV while the pre-edge feature remained essentially unchanged. This suggests that the surface oxide of MnN NPs was slightly reduced at more reducing potentials, but the nitride core remained unaffected. Moreover, the corresponding operando EXAFS spectra in Fig. 3b revealed no substantial changes in Mn–N and Mn–Mn paths (Supplementary Figs. 23 and 24 and Supplementary Table 4), again suggesting that the nitride core remained stable down to 0.50 V.

https://doi.org/10.1038/s41563-024-01998-7

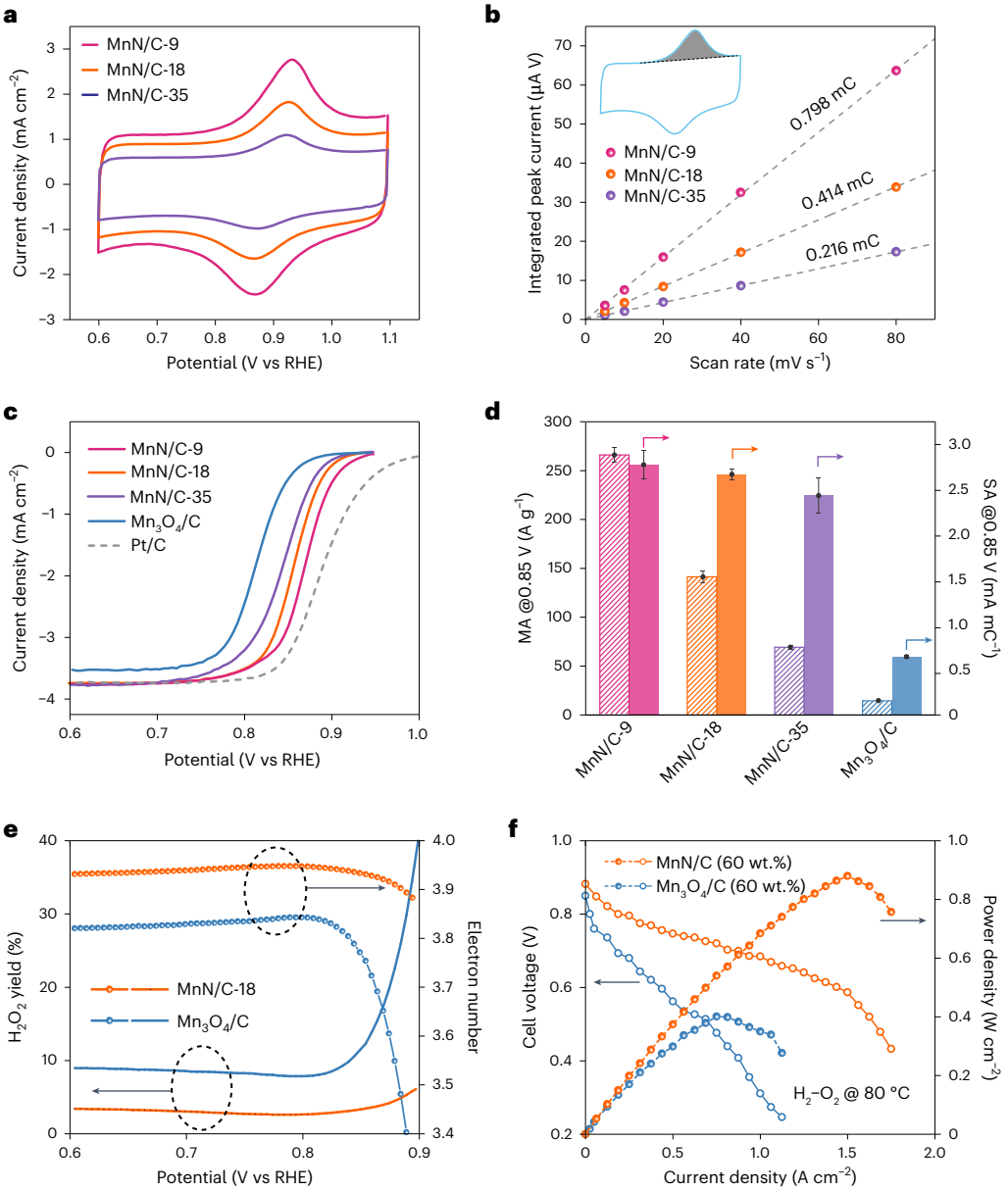

Fig. 2 | Electrochemical evaluation of MnN/C as ORR catalysts in alkaline medium. a, Cyclic voltammograms of MnN/C measured in Ar-saturated 1.0 M KOH solution. Scan rate 40 mV s^{-1}. **b**, Mn(II/III) redox charge determination for MnN/C based on cyclic voltammograms at different scan rates. The grey area of the voltammetric profile was integrated to calculate the charge. **c**, ORR polarization curves of MnN/C, Mn_3O_4/C and commercial Pt/C in O_2-saturated 1.0 M KOH. Scan rate 5 mV s^{-1}; rotation rate 1,600 rpm. Note that this j_{lim} corresponds to 70% of the commonly reported value of 5.5 mA cm^{-2} in 0.1 M KOH[37,38], due to the fact that the oxygen solubility in 1.0 M KOH is 30% lower when compared with its 0.1 M counterpart[39]. **d**, Comparison of MA and specific activity (SA) of MnN/C and Mn_3O_4/C measured at 0.85 V versus RHE. Hatched and solid columns represent the MA and SA, respectively. The MA was normalized to metal loadings while the SA was normalized to the Mn(II/III) redox charges. Data points are presented as mean values and error bars indicate s.d. obtained from triplicate (n = 3) measurements **e**, H_2O_2 yield (bottom region) and electron transfer number (top region) of MnN/C-18 and Mn_3O_4/C, measured with rotating ring disc electrode (RRDE) voltammetry.**f**, AEMFC performance using 60 wt% MnN/C (1.0 mg_{MnN} cm^{-2}) and Mn_3O_4/C (1.0 $mg_{Mn_3O_4}$ cm^{-2}) as cathode and 60 wt.% commercial PtRu/C (0.4 mg_{PtRu} cm^{-2}) anode catalysts. Quaternary ammonium poly(*N*-methyl-piperidine-co-*p*-terphenyl) (QAPPT) was used as the anion exchange membrane. Open and filled circles represent the cell voltage and power density, respectively. Geometric normalization was used to calculate current densities.

However, when the potential was lowered to 0.30 V, the Mn K edge notably shifted to lower energies along with a marked increase in the white line intensity and a substantially abated pre-edge feature (Fig. 3c). These changes may explain the irreversible ORR activity deterioration at potentials below 0.50 V (Supplementary Fig. 25). The EXAFS spectra in Fig. 3d exhibited two distinct scattering shells at radial distances of 1.75 and 2.89 Å, respectively, corresponding to Mn–O and Mn–Mn scattering paths of $Mn(OH)_2$ (Supplementary Fig. 26 and Supplementary Table 4). This result suggests that the conversion to $Mn(OH)_2$ probably proceeded via surface structure degradation followed by irreversible bulk reduction of the MnN phase to Mn(II). The concomitant activity loss suggested that the ORR process is mediated by the Mn(II)/(III) redox transition of surface Mn_3O_4 and should be operated at higher potentials to limit conversion to Mn(II) and maintain structural integrity (Supplementary Fig. 25a). Since $Mn(OH)_2$ is known to be unstable in air and can be converted to other oxides[42], this could explain why $Mn(OH)_2$ was not identified with ex situ techniques (Supplementary Fig. 25b).

https://doi.org/10.1038/s41563-024-01998-7

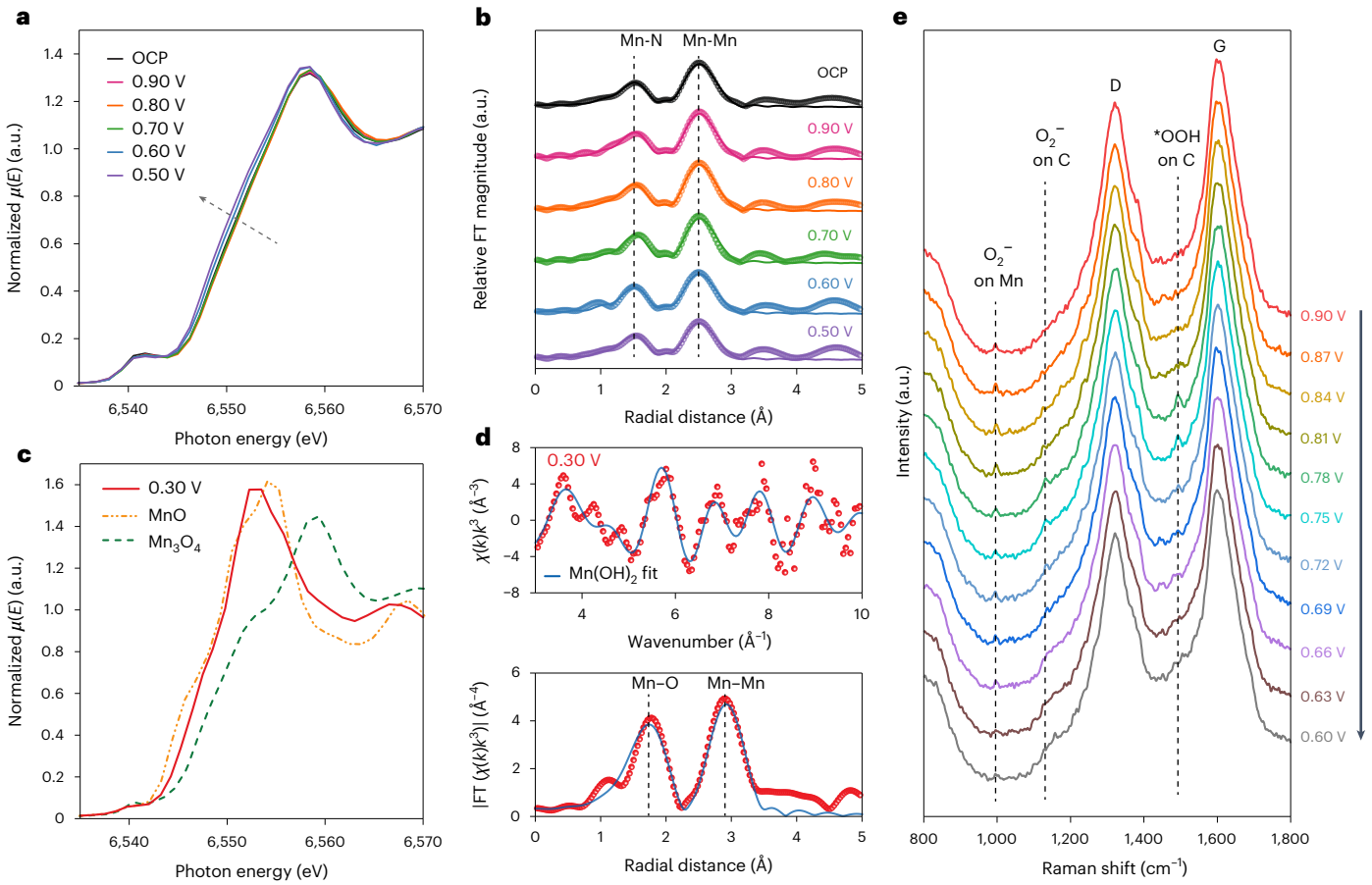

Fig. 3 | Operando/in situ spectroscopic studies of MnN/C under electrochemical conditions. a, Operando Mn K-edge XANES spectra of MnN/C under steady-state conditions from open-circuit potential (OCP, ~1.0 V), followed by applied potentials from 0.90 V to 0.50 V. The dashed arrow indicates a negative shift of the edge energy. **b**, Operando Fourier-transformed EXAFS (circles) and curve fit (lines) for MnN/C. The data are k^3 weighted and not phase corrected. The dashed lines correspond to Mn–N and Mn–Mn coordination shells of MnN, respectively. **c**,**d**, Operando Mn K-edge XANES and EXAFS spectra measured at 0.30 V. **c**, The XANES spectra compared with MnO and Mn_3O_4 references. **d**, The EXAFS spectra in both *k* space and *R* space (FT magnitude component). The dashed lines correspond to Mn–O and Mn–Mn coordination shells of $Mn(OH)_2$. **e**, In situ Raman spectra of MnN/C catalyst at applied potentials from 0.90 V to 0.60 V. The spectra display two major scattering peaks, at 1,322 cm^{-1} and 1,602 cm^{-1}, corresponding to D and G bands from the carbon support. The regions corresponding to O_2^- adsorbed on Mn active sites (996 cm^{-1}), O_2^- on carbon (1,130 cm^{-1}) and *OOH on carbon (1,493 cm^{-1}) are marked by dashed lines. All potentials are referenced to an RHE.

We acquired in situ Raman spectra of the MnN/C catalyst to understand its reaction intermediates and mechanisms during the ORR (Fig. 3e). Three regions are associated with O–O stretching vibrations, which are probably enhanced by the localized surface plasmon resonance in MnN NPs[43]. The first two bands, at about 996 cm^{-1} and 1,130 cm^{-1}, can be ascribed to the superoxide anion species (O_2^-) adsorbed on Mn centres of surface Mn_3O_4 and on carbon, respectively[44]. The other band, at 1,493 cm^{-1}, is ascribed to *OOH adsorbed on carbon. In situ Raman spectra showed that the signal related to O_2^- adsorbed on Mn existed over the entire potential range, indicating that the protonation of $*O_2^-$ to form *OOH could be the rate-determining step of the ORR pathway. Moreover, the emergence of Raman scattering associated with O_2^- and *OOH adsorbed on carbon below 0.81 V suggested that the carbon support probably contributed to the ORR via a two-electron process, as evidenced by the gradual rise of H_2O_2 yield below 0.80 V in Fig. 2e.

Mechanistic analysis of activity

As shown in Fig. 4 and Supplementary Figs. 27–31, we comprehensively analysed how the Mn_3O_4 grew epitaxially on the MnN core. Figure 4c,d presents two atomically resolved STEM images near the surface of a MnN particle viewed along the [100] and [110] axes. In Fig. 4d, the upper phase with a trapezoidal shape displayed lattice spacings and crystal symmetry characteristic of the [100] direction of Mn_3O_4, while the atomic arrangement in the lower part matched well with the projection along the MnN [110] direction. Similarly, Fig. 4c shows an interface from a different zone axis, with atomic-scale features corresponding to Mn_3O_4 [110] and MnN [100] directions for the top and bottom domains, respectively. To help understand the architecture of the near-surface region, we constructed a schematic atomic model based on the atomically resolved STEM images (Fig. 4a,b and Supplementary Fig. 30). Specifically, a truncated pyramid-shaped Mn_3O_4 layer with tetragonal hausmannite structure grew epitaxially on top of a MnN cuboid along the *c* axis ([001] direction), resulting in projection patterns consistent with experimental observations. Using bulk values, the *d*-spacing value of the {200} planes in Mn_3O_4 (2.883 Å) is 3.4% smaller than that of the {220} plane in MnN (2.983 Å) (Supplementary Fig. 30). Thus, to accommodate the difference in the lattice parameter, the Mn_3O_4 layer would experience a tensile strain along the [100] and [010] directions and a compressive strain along the [001] direction, according to a simple elastic strain model (Fig. 4e). This is consistent with the experimentally measured strain of the Mn_3O_4 layer relative to MnN using line profiles from the STEM images (Fig. 4f and Supplementary Fig. 31).

https://doi.org/10.1038/s41563-024-01998-7

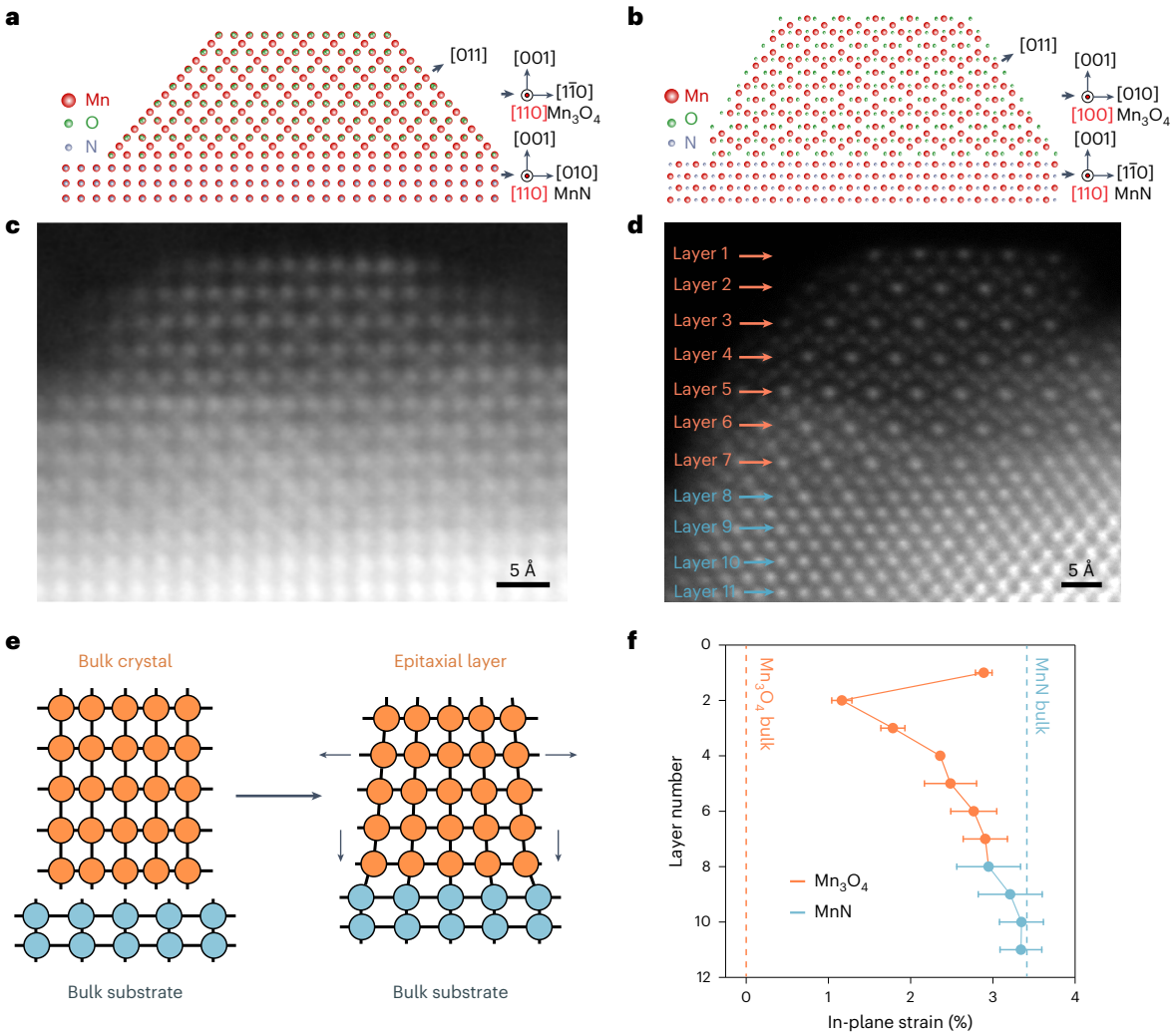

Fig. 4 | Atomic model and strain analysis based on STEM imaging. **a**,**b**, Schematic atomic model of Mn_3O_4 shell and MnN core structure along MnN [100] (**a**) and MnN [110] (**b**). **c**, Atomic-resolution image of MnN along the [100] projection and Mn_3O_4 along the [110] projection. **d**, Atomic-resolution image of MnN along the [110] projection and Mn_3O_4 along the [100] projection. **e**, Schematic illustration of elastic accommodation of strain between epitaxial layer and substrate. **f**, In-plane strain measurements from the atom layers in **d**. An expansive strain relative to the bulk Mn_3O_4 was observed when moving from the core to the shell region, suggesting the presence of a tensile strain in the Mn_3O_4 layer along [010], considering a difference of 3.4% for the fully relaxed oxide structure. The catalyst, after six cycles of ORR tests, was chosen as the subject to incorporate the effect of possible surface reconstruction under electrochemical conditions[49,50]. When compared with the as-synthesized samples, the morphology and elemental distribution of MnN NPs remained virtually unchanged after ORR tests (Supplementary Fig. 27). The strain is determined from the positions of any two neighbouring atoms in each layer. Data points are presented as mean values and error bars indicate s.d. of strain measured within each layer, where the number of replicates (n) depends on the number of atoms and varies between 4 and 15.

To identify how strain in the Mn_3O_4 layer modulated the ORR intermediates and impacted the ORR activity, DFT calculations, which accounted for electrochemical effects using the computational hydrogen electrode framework[45], were performed using the most stable (001) facet of Mn_3O_4 (Supplementary Fig. 32), subject to different applied strains (unstrained, 5% compressed and 5% expanded). We note that the 5% expanded Mn_3O_4(001) surface serves as a first approximation to our MnN/C catalyst, which qualitatively captures the in-plane strain in the top layer of the Mn_3O_4 shell. Binding energies and preferred binding structures for the ORR intermediates (H*, O*, OOH* and OH*) were evaluated at the low-coverage limit of 1/4 monolayer (ML). For each species, nearly identical energetically preferred adsorption structures were observed on all surfaces regardless of level and sign of applied strain (Supplementary Fig. 33). For most of the reaction intermediates, we determined that expansive strain leads to stabilization while compressive strain leads to destabilization of adsorbate binding (Supplementary Table 5)[46–48]. To understand how the adsorption energetics affected the reaction, we constructed Gibbs free-energy diagrams for two possible ORR pathways (OOH* mediated and direct O_2 dissociation) on Mn_3O_4(001) at 0.85 V versus RHE (Fig. 5a). On all these three model surfaces, the direct dissociation pathway was more thermochemically favoured; both pathways are energetically downhill until the formation of OH*. The removal of OH* from the three surfaces ($OH^* \rightarrow (OH^- - e^-) + *$) is the only endergonic step regardless of surface strain (black circles in Fig. 5a). As a compressive strain leads to destabilization of OH* binding (Supplementary Table 5), the OH* removal is made easier (by 0.27 eV) on the 5% compressed Mn_3O_4(001) surface and more difficult (by 0.24 eV) on the 5% expanded Mn_3O_4(001) surface.

The result in Fig. 5a could have two implications. For the ORR occurring at the low-coverage limit, we would expect a compressive strain to favour the ORR activity. However, since the oxide surface was experimentally determined to experience an expansive strain, this should lead to the stabilization of OH* binding and potentially to a more hydroxylated surface. The latter is consistent with our experimental

https://doi.org/10.1038/s41563-024-01998-7

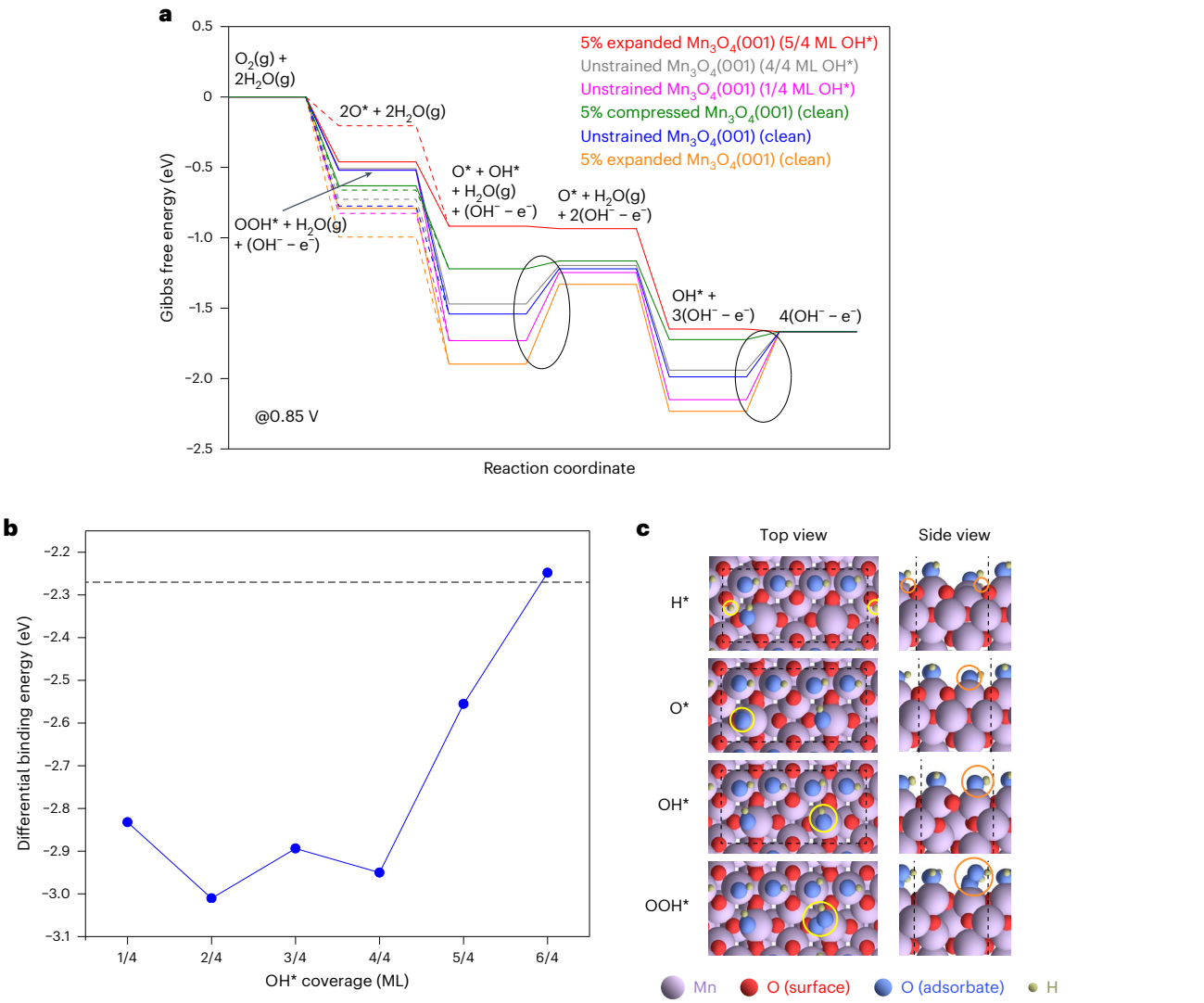

Fig. 5 | DFT calculations to understand the strain effects on ORR performance. a, Gibbs free-energy diagram of the ORR process on clean unstrained, 5% compressed and 5% expanded $Mn_3O_4(001)$ surfaces as well as on 5% expanded $Mn_3O_4(001)$ covered with 5/4 ML OH* spectator species and unstrained $Mn_3O_4(001)$ covered with 4/4 ML and 1/4 ML OH* spectator species at 0.85 V versus RHE, considering both OOH*-mediated (solid) and direct dissociation (dashed) pathways. Black ellipses denote the OH* removal step ($OH^* \rightarrow (OH^- - e^-) + *$). All energetics were obtained at the low-coverage limit of 1/4 ML for each of the active intermediates. **b**, Differential binding energy of OH* as a function of its surface coverage on 5% expanded $Mn_3O_4(001)$. The horizontal black dashed line denotes a differential binding energy value of −2.27 eV, when an adsorbed OH* is in equilibrium with $(OH^- - e^-)$ at 0.85 V versus RHE. When the OH* coverage increases to 6/4 ML, the differential binding energy of the sixth OH* in the unit cell becomes −2.25 eV, at which point the desorption of OH* from the surface ($OH^* \rightarrow (OH^- - e^-) + *$) is exergonic by 0.02 eV at 0.85 V versus RHE. **c**, Top and side views of the preferred (lowest-energy) binding structures of adsorbed intermediates (H*, O*, OH* and OOH*) on the 5% expanded $Mn_3O_4(001)$ surface in the presence of 5/4 ML OH* spectator species. Yellow and orange circles indicate the adsorbates of interest for each panel. Dashed lines denote the (2 × 1) unit cell.

observations from cyclic voltammetry measurements (Supplementary Fig. 34 and Supplementary Notes), from which we estimated the OH* coverage on the MnN/C catalyst (which exhibits an expansively strained Mn_3O_4 surface) to be as much as five times the OH* coverage on the Mn_3O_4/C catalyst (that is, the unstrained Mn_3O_4 surface). Accordingly, and to probe the effect of the degree of hydroxylation of $Mn_3O_4(001)$ on its ORR activity, we first examined the OH* adsorption on a 5% expanded $Mn_3O_4(001)$ surface at increasing OH* coverages (Fig. 5b and Supplementary Fig. 35). Up to 4/4 ML OH* coverage, OH* preferentially binds on the protruding rows of Mn atoms on the $Mn_3O_4(001)$ surface until they become fully covered (Supplementary Fig. 35), and the adsorption of OH* is stabilized, compared with that at the low-coverage limit (1/4 ML; Fig. 5b). Above 4/4 ML OH* coverage, additional OH* species will have to be adsorbed on the Mn atoms embedded in the 'grooves' between the protruding Mn rows (Supplementary Fig. 35), and notably destabilized. As shown in Fig. 5b, 5/4 ML is the highest OH* coverage at which the OH* adsorption ($(OH^- - e^-) + * \rightarrow OH^*$) is endergonic, by 0.02 eV at 0.85 V versus RHE.

Consequently, 5/4 ML OH*-covered $Mn_3O_4(001)$ was chosen as a representative model for the 5% expanded Mn_3O_4 surface under ORR conditions. We used that model to study the adsorption of ORR intermediates (H*, O*, OH* and OOH*; Fig. 5c and Supplementary Table 5). The resulting Gibbs free-energy diagram is shown in Fig. 5a (red lines). In the presence of 5/4 ML OH* spectator species, the energy diagram becomes energetically downhill. Notably, the OH* removal step (Fig. 5a) is no longer endergonic. Also, on the 5/4 ML OH-covered 5% expanded $Mn_3O_4(001)$ surface, the OOH pathway becomes energetically favourable over the direct O_2 dissociation pathway. Further, we evaluated the Gibbs free-energy diagrams on the unstrained $Mn_3O_4(001)$ surface covered by OH* at coverages lower than 5/4 ML (1/4 ML, which

corresponds to the fivefold OH* coverage difference predicted by our cyclic voltammetry analysis, and 4/4 ML, denoted by pink and grey lines in Fig. 5a, respectively). Note that on the 1/4 ML and 4/4 ML OH-covered unstrained Mn_3O_4(001) surface, the OH* removal step (black circles in Fig. 5a) is still endergonic. We conclude that the superior intrinsic ORR activity of our MnN catalyst probably originates from an expanded oxide surface that is more hydroxylated than unstrained Mn_3O_4, whereby a higher surface coverage of OH* facilitates its removal. A more detailed atomistic model could benefit from further knowledge of the surface OH* coverage, accounting for possible oxide formation and the inclusion of the nitride substrate. Nonetheless, our current work provides a valuable atomic-scale understanding of the nitride/oxide interface in TMNs and showcases control of surface hydroxylation as an effective approach to manipulate the electrochemical properties of Mn_3O_4 and of other transition metal oxides more broadly.

Online content

Any methods, additional references, Nature Portfolio reporting summaries, source data, extended data, supplementary information, acknowledgements, peer review information; details of author contributions and competing interests; and statements of data and code availability are available at https://doi.org/10.1038/s41563-024-01998-7.

References

1. Debe, M. K. Electrocatalyst approaches and challenges for automotive fuel cells. *Nature* **486**, 43–51 (2012).
2. Shao, M., Chang, Q., Dodelet, J.-P. & Chenitz, R. Recent advances in electrocatalysts for oxygen reduction reaction. *Chem. Rev.* **116**, 3594–3657 (2016).
3. Yarlagadda, V. et al. Boosting fuel cell performance with accessible carbon mesopores. *ACS Energy Lett.* **3**, 618–621 (2018).
4. Jaganmohan, M. Mine production of platinum worldwide from 2010 to 2021. *Statista* https://www.statista.com/statistics/1170691/mine-production-of-platinum-worldwide/ (2024).
5. Lu, S., Pan, J., Huang, A., Zhuang, L. & Lu, J. Alkaline polymer electrolyte fuel cells completely free from noble metal catalysts. *Proc. Natl Acad. Sci. USA* **105**, 20611–20614 (2008).
6. Yang, Y. et al. Electrocatalysis in alkaline media and alkaline membrane-based energy technologies. *Chem. Rev.* **122**, 6117–6321 (2022).
7. Ni, W. et al. An efficient nickel hydrogen oxidation catalyst for hydroxide exchange membrane fuel cells. *Nat. Mater.* **21**, 804–810 (2022).
8. Zhao, Q., Yan, Z., Chen, C. & Chen, J. Spinels: controlled preparation, oxygen reduction/evolution reaction application, and beyond. *Chem. Rev.* **117**, 10121–10211 (2017).
9. Hong, W. T. et al. Toward the rational design of non-precious transition metal oxides for oxygen electrocatalysis. *Energy Environ. Sci.* **8**, 1404–1427 (2015).
10. Wang, Y., Li, J. & Wei, Z. Transition-metal-oxide-based catalysts for the oxygen reduction reaction. *J. Mater. Chem. A* **6**, 8194–8209 (2018).
11. Liang, Y. et al. Co_3O_4 nanocrystals on graphene as a synergistic catalyst for oxygen reduction reaction. *Nat. Mater.* **10**, 780–786 (2011).
12. Tong, Y. et al. A bifunctional hybrid electrocatalyst for oxygen reduction and evolution: cobalt oxide nanoparticles strongly coupled to B,N-decorated graphene. *Angew. Chem.* **56**, 7121–7125 (2017).
13. Gorlin, Y., Chung, C. J., Nordlund, D., Clemens, B. M. & Jaramillo, T. F. Mn_3O_4 supported on glassy carbon: an active non-precious metal catalyst for the oxygen reduction reaction. *ACS Catal.* **2**, 2687–2694 (2012).
14. Stoerzinger, K. A., Risch, M., Han, B. & Shao-Horn, Y. Recent insights into manganese oxides in catalyzing oxygen reduction kinetics. *ACS Catal.* **5**, 6021–6031 (2015).
15. Wang, Y. et al. Synergistic Mn–Co catalyst outperforms Pt on high-rate oxygen reduction for alkaline polymer electrolyte fuel cells. *Nat. Commun.* **10**, 1506 (2019).
16. Zhou, Y. et al. Revealing the dominant chemistry for oxygen reduction reaction on small oxide nanoparticles. *ACS Catal.* **8**, 673–677 (2018).
17. Yang, Y. et al. Octahedral spinel electrocatalysts for alkaline fuel cells. *Proc. Natl Acad. Sci. USA* **116**, 24425–24432 (2019).
18. Yang, Y. et al. Epitaxial thin-film spinel oxides as oxygen reduction electrocatalysts in alkaline media. *Chem. Mater.* **33**, 4006–4013 (2021).
19. Bredar, A. R C. et al. Oxygen reduction electrocatalysis with epitaxially grown spinel $MnFe_2O_4$ and Fe_3O_4. *ACS Catal.* **12**, 3577–3588 (2022).
20. Zheng, J. et al. Recent advances in nanostructured transition metal nitrides for fuel cells. *J. Mater. Chem. A* **8**, 20803–20818 (2020).
21. Wang, H. et al. Transition metal nitrides for electrochemical energy applications. *Chem. Soc. Rev.* **50**, 1354–1390 (2021).
22. Chen, P. et al. Metallic Co_4N porous nanowire arrays activated by surface oxidation as electrocatalysts for the oxygen evolution reaction. *Angew. Chem.* **54**, 14710–14714 (2015).
23. Walter, C. et al. A molecular approach to manganese nitride acting as a high performance electrocatalyst in the oxygen evolution reaction. *Angew. Chem.* **57**, 698–702 (2018).
24. Yang, Y., Zeng, R., Xiong, Y., Disalvo, F. J. & Abruña, H. D. Cobalt-based nitride-core oxide-shell oxygen reduction electrocatalysts. *J. Am. Chem. Soc.* **141**, 19241–19245 (2019).
25. Luo, J. et al. Limitations and improvement strategies for early-transition-metal nitrides as competitive catalysts toward the oxygen reduction reaction. *ACS Catal.* **6**, 6165–6174 (2016).
26. Miura, A. et al. Nitrogen-rich manganese oxynitrides with enhanced catalytic activity in the oxygen reduction reaction. *Angew. Chem.* **55**, 7963–7967 (2016).
27. Tian, X. L. et al. Formation of a tubular assembly by ultrathin $Ti_{0.8}Co_{0.2}N$ nanosheets as efficient oxygen reduction electrocatalysts for hydrogen–/metal–air fuel cells. *ACS Catal.* **8**, 8970–8975 (2018).
28. Yuan, Y. et al. Zirconium nitride catalysts surpass platinum for oxygen reduction. *Nat. Mater.* **19**, 282–286 (2020).
29. Zeng, R. et al. Non-precious transition metal nitrides as efficient oxygen reduction electrocatalysts for alkaline fuel cells. *Sci. Adv.* **8**, eabj1584 (2022).
30. Deng, Y.-P. et al. Dynamic electrocatalyst with current-driven oxyhydroxide shell for rechargeable zinc–air battery. *Nat. Commun.* **11**, 1952 (2020).
31. Yang, H., Al-Brithen, H., Trifan, E., Ingram, D. C. & Smith, A. R. Crystalline phase and orientation control of manganese nitride grown on MgO(001) by molecular beam epitaxy. *J. Appl. Phys.* **91**, 1053–1059 (2002).
32. Sun, W. et al. Thermodynamic routes to novel metastable nitrogen-rich nitrides. *Chem. Mater.* **29**, 6936–6946 (2017).
33. Leineweber, A., Niewa, R., Jacobs, H. & Kockelmann, W. The manganese nitrides η-Mn_3N_2 and θ-$Mn_6N_{(5+x)}$: nuclear and magnetic structures. *J. Mater. Chem.* **10**, 2827–2834 (2000).
34. Timoshenko, J. & Roldan Cuenya, B. In situ/operando electrocatalyst characterization by X-ray absorption spectroscopy. *Chem. Rev.* **121**, 882–961 (2021).
35. Wang, M. & Feng, Z. Pitfalls in X-ray absorption spectroscopy analysis and interpretation: a practical guide for general users. *Curr. Opin. Electrochem.* **30**, 100803 (2021).
36. Wei, C. et al. Approaches for measuring the surface areas of metal oxide electrocatalysts for determining their intrinsic electrocatalytic activity. *Chem. Soc. Rev.* **48**, 2518–2534 (2019).

37. Wang, L. et al. Tunable intrinsic strain in two-dimensional transition metal electrocatalysts. *Science* **363**, 870–874 (2019).
38. Li, H. et al. Oxidative stability matters: a case study of palladium hydride nanosheets for alkaline fuel cells. *J. Am. Chem. Soc.* **144**, 8106–8114 (2022).
39. Davis, R. E., Horvath, G. L. & Tobias, C. W. The solubility and diffusion coefficient of oxygen in potassium hydroxide solutions. *Electrochim. Acta* **12**, 287–297 (1967).
40. Fan, J. et al. Bridging the gap between highly active oxygen reduction reaction catalysts and effective catalyst layers for proton exchange membrane fuel cells. *Nat. Energy* **6**, 475–486 (2021).
41. Yang, Y. et al. High-loading composition-tolerant Co–Mn spinel oxides with performance beyond 1 W/cm^2 in alkaline polymer electrolyte fuel cells. *ACS Energy Lett.* **4**, 1251–1257 (2019).
42. Noda, N. et al. Highly oxidizing aqueous environments on early Mars inferred from scavenging pattern of trace metals on manganese oxides. *J. Geophys. Res. Planets* **124**, 1282–1295 (2019).
43. Dasog, M. Transition metal nitrides are heating up the field of plasmonics. *Chem. Mater.* **34**, 4249–4258 (2022).
44. Wei, J. et al. Probing the oxygen reduction reaction intermediates and dynamic active site structures of molecular and pyrolyzed Fe–N–C electrocatalysts by in situ Raman spectroscopy. *ACS Catal.* **12**, 7811–7820 (2022).
45. Nørskov, J. K. et al. Origin of the overpotential for oxygen reduction at a fuel-cell cathode. *J. Phys. Chem. B* **108**, 17886–17892 (2004).
46. Mavrikakis, M., Hammer, B. & Nørskov, J. K. Effect of strain on the reactivity of metal surfaces. *Phys. Rev. Lett.* **81**, 2819–2822 (1998).
47. Han, J. W. & Yildiz, B. Mechanism for enhanced oxygen reduction kinetics at the (La,Sr)$CoO_{3-\delta}$/(La,Sr)$_2CoO_{4+\delta}$ hetero-interface. *Energy Environ. Sci.* **5**, 8598–8607 (2012).
48. Ma, D. et al. Effect of lattice strain on the oxygen vacancy formation and hydrogen adsorption at CeO_2(111) surface. *Phys. Lett. A* **378**, 2570–2575 (2014).
49. Zeng, Y. et al. Surface reconstruction of water splitting electrocatalysts. *Adv. Energy Mater.* **12**, 2201713 (2022).
50. Mefford, J. T. et al. Correlative operando microscopy of oxygen evolution electrocatalysts. *Nature* **593**, 67–73 (2021).

Methods

Catalyst synthesis

Considering a lack of effective synthesis methods in the literature[23,26,29], we introduced a simple one-step nitridation strategy by annealing carbon-supported manganese precursors in an ammonia environment. The carbon support was introduced to fully disperse the MnN NPs and thus maximize catalyst utilization. This strategy avoided complicated synthesis procedures and required no surfactant, capping agent or organic solvent, and hence is also environmentally friendly. A targeted 600 °C nitridation temperature was required for complete conversion of the manganese precursors into the nitride phase (Supplementary Fig. 2). In a typical synthesis of MnN/C-18, 0.3 mmol manganese(II) acetate tetrahydrate ($(CH_3COO)_2Mn{\cdot}4H_2O$, ≥99.0%, Sigma-Aldrich) was first dissolved in 0.6 ml H_2O under magnetic stirring and then used to impregnate high-surface-area Ketjen Black carbon powder (EC-600JD, AkzoNobel) in small aliquots. For a targeted nitride loading (20 wt%), 100 mg of carbon powder was used. The wet sample was frozen with liquid nitrogen and then dried in a freeze dryer for 24 h. The resulting precursor was then ground into powder in an agate mortar, transferred into an alumina ceramic boat and annealed at 600 °C with flowing ammonia gas (100 ml min^{-1}) in a tubular furnace. After a 2 h nitridation process, the sample was cooled to room temperature and ground into powder. MnN/C-9 was synthesized with the same heating cycles as for MnN/C-18, but the precursor was kept in an Ar-purged desiccator for over a month before nitridation. MnN/C-35 was synthesized with 0.3 mmol manganese(II) nitrate hydrate ($Mn(NO_3)_2{\cdot}xH_2O$, ≥99.99%, Sigma-Aldrich) and treated under similar conditions as for MnN/C-18. The Mn_3O_4/C catalyst was synthesized following a facile hydrothermal method, as reported in previous work[17].

Structural and morphological characterizations

XRD patterns of MnN/C catalysts were collected from 30° to 85° at a scan rate of 4° min^{-1} and step size of 0.02° on a Rigaku Ultima IV diffractometer (Cu Kα, λ = 1.5406 Å) operated at 1.76 kW (40 kV and 44 mA). The background subtraction was performed with Rigaku PDXL software. X-ray absorption fine structure spectra of the Mn K edge were recorded in transmission mode (from 6,400 to 7,100 eV) at the PIPOX beamline of the Cornell High Energy Synchrotron Source. The powder sample was fully mixed with boron nitride before loading onto a holder for measurement. The spectra were calibrated against the absorption edge (maximum of first derivative) of Mn metal foils at 6,539.0 eV and processed with ATHENA and ARTEMIS software packages[51]. The samples for TEM characterization were prepared by dropping a sample suspension onto a lacy carbon TEM grid (Electron Microscopy Science, 200 mesh, copper grid), which was dried under an infrared lamp and then baked out under vacuum (1.3×10^{-7} torr) at 120 °C for 7 h to remove contaminants. Morphology and particle size distribution analysis of as-prepared samples were investigated with a FEI Tecnai F20 TEM/STEM operated at 200 kV with a convergence angle of 7–10 mrad. The high-magnification STEM experiment was conducted with a Thermo Scientific Spectra 300 Ultra CFEG S/TEM operated at 120 kV with 0.78 Å resolution. The atomic-scale images were acquired with a spot size of 6, C2 aperture of 70 µm, camera length of 100 mm and convergence angle of 30 mrad with both high-angle angular dark-field and bright-field detectors simultaneously. Additional details of the high-magnification STEM experiment can be found in Supplementary Methods. The projected atomic models were generated using VESTA software on the basis of a standard crystal database. The EELS spectra were fitted with a linear combination of power laws with the background at 50 eV before the edge onset. The Mn elemental maps were acquired from L_3 and L_2 edges from EELS data while K edges were used for N and O elemental maps. All the elemental maps were processed with principal component analysis with three components with the CSI plugin in ImageJ software[52]. X-ray photoemission spectra were obtained with a Scienta Omicron ESCA-2SR spectrometer equipped with a monochromatic Al Kα radiation source (1,486.6 eV). Photoelectrons were recorded at a 0° emission angle with a source to analyser angle of 54.7°. The electron kinetic energy was determined with a hemispherical analyser, with a pass energy of 200 eV and 50 eV for survey and high-resolution scans, respectively.

Electrochemical measurements

RDE and RRDE measurements were carried out in a polyethylene three-electrode electrochemical cell with a WaveDriver 10 potentiostat system from Pine Instruments. The three-electrode cell was cleaned with aqua regia and rinsed with deionized water three times before electrochemical measurements. A porous graphite rod served as the counter-electrode while a Ag/AgCl (saturated KCl) electrode was used as the reference electrode. To minimize the potential impact from the reference electrode shift, the reference potentials were examined in saturated KCl solution before and after electrochemical measurements (Supplementary Fig. 36). It should be noted that the best experimental practice is to use a Hg/HgO reference electrode under alkaline conditions. While it was not used here, the potential stability of the Ag/AgCl reference electrode was demonstrated in this study (Supplementary Fig. 36) to be less than 2 mV. The potential of the reference electrode was calibrated to the RHE scale on the basis of $E_{RHE} = E_{Ag/AgCl} + 1.023$ V, as determined in Supplementary Figs. 37 and 38. The thin-film working electrode was prepared with catalyst ink by the drop-casting method. MnN/C catalysts (20 wt%) were dispersed into Nafion/ethanol (0.25 wt%) solution under sonication and then drop-cast onto an RDE electrode (glassy carbon disc 0.1964 cm^2) to achieve a loading of 50 µg cm^{-2}. Cyclic voltammetry profiles at different scan rates were obtained in ultrahigh-purity Ar-saturated 1.0 M KOH solution over the potential range of 0.6–1.1 V versus RHE. ORR polarization curves were acquired in ultrahigh-purity O_2 saturated electrolyte over the potential range of 0.6–0.95 V versus RHE at a scan rate of 5 mV s^{-1} and rotation rate of 1,600 r.p.m. The current density was calculated on the basis of the geometric area of the working electrode (0.1964 cm^2). For ORR selectivity evaluation using the RRDE method (glassy carbon disc 0.2475 cm^2 + Pt ring 0.1866 cm^2), the measurements were conducted under similar conditions to the RDE set-up. Before the measurement, the Pt ring was cycled between 0.05 and 1.20 V versus RHE at a scan rate of 50 mV s^{-1} until a stable profile was obtained. The side product (H_2O_2) generated from the working electrode was collected at the Pt ring (@1.30 V versus RHE) with a collection efficiency of 37%. The calculation of H_2O_2 yield and electron number can be found in ref. 17. The ORR durability testing was conducted following an accelerated durability testing protocol: potential cycling between 0.60 and 0.95 V versus RHE for 10,000 cycles in O_2-saturated 1.0 M KOH solution. To eliminate the impact of the potential shift due to extended accelerated durability testing runs, two sets of Ag/AgCl reference electrodes were used in this study: one for the long-term durability tests, another for short-term RDE measurements. By doing so, we aimed to minimize any potential impact from the reference electrode shift on the electrochemical performance. All electrochemical data were processed without ohmic resistance compensation.

The AEMFC performance evaluation of the MnN/C cathode was based on the catalyst-coated membrane technique using a QAPPT (Alkymer, ion-exchange capacity 2.50 ± 0.05 mmol g^{-1}, 25 ± 2 µm thick) membrane and ionomer binder, purchased from EVE Institute of New Energy Technology. Additional details of testing procedures can be found in Supplementary Methods.

Operando XAS measurement and analysis

MnN/C (20 wt%) was first dispersed in a Nafion/ethanol (0.25 wt%) solution and then drop-cast onto one end (1 × 1 cm^2) of a 1 × 5 cm^2 piece of carbon paper (AvCarb MGL190, Fuel Cell Store). The carbon

paper served as a non-active conductor with negligible effects on the catalytic current. The loading of the MnN catalyst layer was controlled to 0.4 mg cm^{-2} to ensure adequate signal but also low enough thickness to avoid possible self-absorption. The details of the electrochemical cell used for operando XAS measurements can be found in our previous work[53]. In brief, the cell was made of two chemically inert polyether ether ketone (McMaster-Carr) sheets with a Kapton window in the middle (diameter 10 mm). The electrolyte thickness was adjusted to less than 200 μm by placing a Viton U-shaped sealing cord between the two polyether ether ketone pieces. A polyether ether ketone cap with one gas inlet and one gas outlet on top of the cell was used to bubble O_2 gas through during the measurement. The catalyst side of the carbon paper was immersed into the electrolyte, acting as the working electrode. Similar to the three-electrode system for catalyst evaluation, a porous graphite rod (counter-electrode) was placed near the working electrode while a Ag/AgCl reference electrode with saturated KCl was connected to the cell via a salt bridge to minimize the voltage drop. A potentiostat from Pine Instruments was used for operando X-ray data acquisition. The operando XAS spectra at the Mn K edge were recorded in fluorescence mode at the PIPOXS beamline of the Cornell High Energy Synchrotron Source under ring conditions of 100 mA at 6 GeV. The incident beam was energy selected using a liquid-nitrogen-cooled Si(111) monochromator and focused to a spot of 1.0 mm × 0.7 mm using a pair of Rh-coated focusing mirrors. Data were acquired from 6,400 to 7,100 eV and detected using a four-element Vortex detector positioned at 90° relative to the sample; data were averaged from seven scans to enhance the signal-to-noise ratio. Beam damage of the catalyst was routinely examined before and after measurement. The XANES spectra were calibrated against the absorption edge (maximum of first derivative) of Mn metal foils at 6,539.0 eV and processed with the ATHENA and ARTEMIS software packages[51]. Fourier-transformed EXAFS spectra were plotted by applying a Hanning window from 3 to 11 $Å^{-1}$ with k^3 weighting and no phase correction. The EXAFS spectrum of MnN/C catalysts was fitted with the standard crystal structure ($Mn_6N_{5.26}$, Inorganic Crystal Structure Database no. 290804)[33].

In situ Raman spectroscopy measurements and analysis

MnN/C (20 wt%) was first dispersed in a Nafion/ethanol (0.25 wt%) solution and then drop-cast onto a glassy carbon disc electrode (diameter 3 mm, CH Instruments) and placed in a home-made quartz-window electrochemical spectroscopic Raman cell (three electrodes, graphite as counter-electrode, Ag/AgCl in 1.0 M KCl as reference electrode). The electrochemical parameters were controlled using an electrochemical workstation (CHI1205c, CH Instruments). A home-built optical system was utilized for in situ electrochemical Raman measurements. A He–Ne 632.8 nm laser (Thorlabs HNL210LB) and a ×10 objective (Olympus Plan Achromat, 0.25 numerical aperture, 10.6 mm working distance, Thorlabs, RMS10X) were used as a laser source and for signal collection respectively. The average power was kept around 1.7 mW or below (on sample) to avoid possible damage during the measurements. The collected Raman signal was finally dispersed using a spectrograph (Shamrock, Andor) and detected using an electron-multiplied CCD (charge-coupled device, Newton, Andor). The obtained Raman spectra were directly plotted in Origin Pro from 800 cm^{-1} to 1,800 cm^{-1} in arbitrary units with no background or spectrum subtraction.

Computational methods

All the DFT calculations were conducted using the Vienna Ab Initio Simulation Package[54,55]. Additional computational details can be found in Supplementary Methods.

Data availability

The data supporting the findings of this study are included in the published article and its Supplementary Information or available from the corresponding authors on request. Source data are provided with this paper.

References

51. Ravel, B. & Newville, M. ATHENA, ARTEMIS, HEPHAESTUS: data analysis for X-ray absorption spectroscopy using IFEFFIT. *J. Synchrotron Radiat.* **12**, 537–541 (2005).
52. Cueva, P., Hovden, R., Mundy, J. A., Xin, H. L. & Muller, D. A. Data processing for atomic resolution electron energy loss spectroscopy. *Microsc. Microanal.* **18**, 667–675 (2012).
53. Yang, Y. et al. *In situ* X-ray absorption spectroscopy of a synergistic Co–Mn oxide catalyst for the oxygen reduction reaction. *J. Am. Chem. Soc.* **141**, 1463–1466 (2019).
54. Kresse, G. & Furthmüller, J. Efficient iterative schemes for *ab initio* total-energy calculations using a plane-wave basis set. *Phys. Rev. B* **54**, 11186 (1996).
55. Kresse, G. & Furthmüller, J. Efficiency of ab-initio total energy calculations for metals and semiconductors using a plane-wave basis set. *Comput. Mater. Sci.* **6**, 15–50 (1996).

Acknowledgements

This work was supported by the Center for Alkaline Based Energy Solutions (CABES), part of the Energy Frontier Research Center (EFRC) programme supported by the US Department of Energy under Grant DE-SC-0019445 (R.Z., H.L., Z.S., L.X., W.X., H.W., Q.L., M.M., D.M., H.D.A.). This work made use of TEM facilities at the Cornell Center for Materials Research (CCMR), which are supported through the National Science Foundation Materials Research Science and Engineering Center (NSF MRSEC) programme (DMR1719875, Z.S., D.M.) and PARADIM, an NSF MIP (DMR-2039380, Z.S., D.M.). This research used resources of the National Energy Research Scientific Computing Center, a DOE Office of Science User Facility supported by the Office of Science of the US Department of Energy under Contract DE-AC02-05CH11231 (L.X., M.M.) using NERSC award BES-ERCAP0022773. The in situ Raman measurement is supported by the Air Force Office of Scientific Research under award numbers FA9550-18-1-0420 (J.M, T.L.) This work is based on research conducted at the Center for High-Energy X-ray Sciences (CHEXS), which is supported by the National Science Foundation (BIO, ENG and MPS Directorates) under award DMR-1829070 (C.J.P.). We thank F. J. DiSalvo for helpful suggestions on material synthesis. We are also grateful to J. Grazul and M. Thomas at CCMR for the help in STEM training. We appreciate the assistance of Cornell High Energy Synchrotron Source staff scientists at the PIPOXS beamline, L. Debefve and K. D. Finkelstein.

Author contributions

R.Z., H.L. and H.D.A. conceived and designed the experiments. R.Z. and H.L. performed sample preparation, XRD, XAS and X-ray photoemission spectroscopy characterization and the electrochemical measurements with assistance from H.W. Z.S. conducted STEM-EELS characterization and strain analysis, supervised by D.M. R.Z. and H.L. performed operando XAS characterization and data analysis with the help of W.X. and C.J.P. J.M. carried out in situ Raman spectroscopy characterization and data analysis, supervised by T.L. L.X. and M.M. conceived and designed the modelling work and L.X. performed the DFT calculations. R.Z. and H.L. carried out membrane electrode assembly testing with the help of Q.L. R.Z., H.L., Z.S., L.X., M.M. and H.D.A. wrote the paper. All of the authors discussed the results and commented on the paper.

Competing interests

The authors declare no competing interests.

Additional information

Supplementary information The online version contains supplementary material available at https://doi.org/10.1038/s41563-024-01998-7.

Correspondence and requests for materials should be addressed to Tianquan Lian, Manos Mavrikakis, David A. Muller or Héctor D. Abruña.

Peer review information *Nature Materials* thanks the anonymous reviewers for their contribution to the peer review of this work.